CHAPTER 5

FATIGUE AND CHARPY IMPACT BEHAVIOUR

In this chapter, we present the impact of a higher volume fraction of retained austenite on the low cycle fatigue (LCF) behaviour at room temperature, as well as the Charpy impact behaviour at three distinct temperatures: room temperature, 0°C, and -40°C. Specifically, we investigate these effects in a high carbon, high silicon carbide-free nanostructured bainitic steel. This chapter deals with significant insights into the influence of a higher volume fraction of retained austenite, combined with bainite, on the fracture behaviour of carbide-free nanostructured bainitic steel samples. The findings presented herein are of great value and can contribute to the design and optimization of manufacturing processes for high-performance applications that encounter cyclic loading and impact loading conditions.

5.1 LOW CYCLE FATIGUE BEHAVIOUR

5.1.1 Cyclic Stress Response

The cyclic stress response of the austempered sample B12VA-2 exhibits notable behaviour under varying strain amplitudes (Figure 5.1). The results indicate a trend of initial moderate hardening, particularly noticeable at lower strain amplitudes of ±0.50% and ±0.60%. This hardening process occurs relatively quickly, typically within the first 100 cycles. Interestingly, the hardening phenomenon at higher strain amplitudes of ±0.70% and ±0.80% is even more rapid. In these cases, the sample experiences significant hardening within just a few cycles, usually less than 10. Once the initial hardening phase is complete, the cyclic stress remains relatively constant over a substantial number of subsequent cycles.

This suggests that the material reaches a stabilized state, where the stress experienced during each cycle does not vary significantly. However, despite the stabilized cyclic stress, the material ultimately fractures at the end of the cyclic loading regime. The degree of cyclic hardening increases as the strain amplitude rises. This implies that higher strain amplitudes lead to more pronounced hardening during the cyclic loading process. In summary, the austempered sample B12VA-2 demonstrates distinct cyclic stress response patterns under different strain amplitudes, with varying rates of hardening and ultimately leading to fracture. The fatigue life of B12VA-2 samples decreases with increasing strain amplitudes.

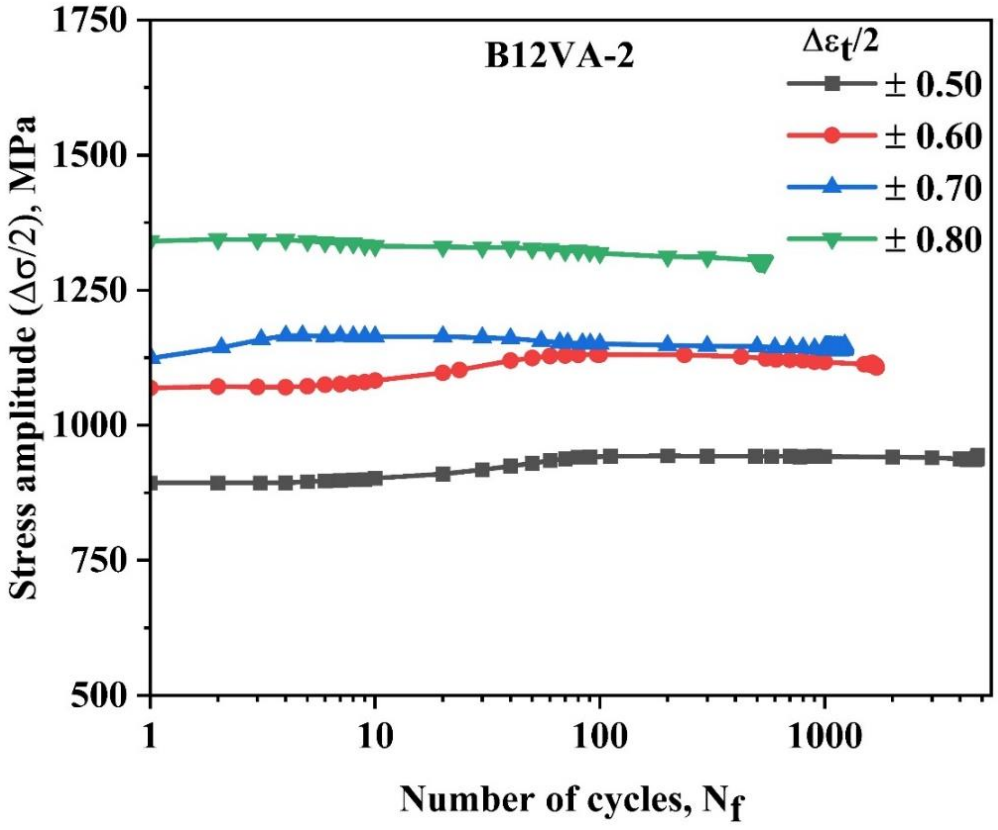

Figure 5.1 Cyclic stress response of austempered samples B12VA-2.

Figure 5.2 depicts cyclic stress response of the sample B14VA-2, and its fatigue behaviour is observed to be similar to that of sample B12VA-2. Cyclic hardening occurs

in just 100 cycles at lower strain amplitudes of ±0.50 and ±0.60 and at higher strain amplitude it occurs within few cycles. Sample B14VA-2 displays a unique cyclic stress response other than sample B12VA-2. Initially, there is cyclic hardening, followed by subsequent softening over a large number of cycles. Towards the end, a very small stress drop occurs, prior to fracture.

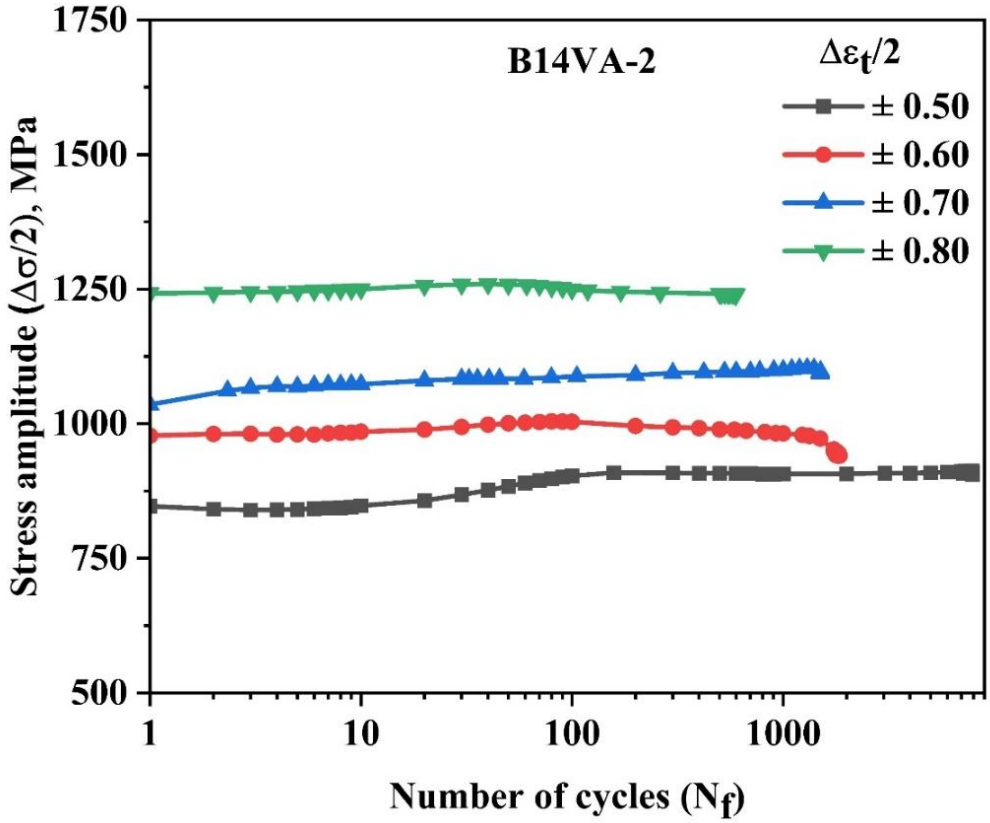

Figure 5.2 Cyclic stress response of austempered sample B14VA-2.

The cyclic stress response of B15VA-2 sample is shown in Figure 5.3. Higher degree of cyclic hardening than B12VA-2 and B14VA-2 is observed. The hardening occurs at around 100 cycles at ±0.50 strain amplitude and with increasing strain amplitude gradual hardening occurs in around 70-80 cycles. Further, cyclic softening was observed at higher strain amplitude (±0.60 to ±0.80) in this material. In contrast, in the sample B15VA-2, at higher strain amplitude, there is cyclic hardening during the initial

cycles and softening in the subsequent large number of cycles, followed by rapid drop during the last stage leading to fracture.

The material B12VA-2 shows fatigue life of 4777 cycles at ±0.50 strain amplitude and it decreases to 539 cycles with increasing strain amplitude (±0.80) as depicted in Figure 5.4. The sample B14VA-2 reveals fatigue life of 7899 cycles at ±0.50 strain amplitude and it reduces to 599 cycles at ±0.80 strain amplitude. Further, material B15VA-2 delivers best fatigue life of 11322 cycles at ±0.50 strain amplitude and 864 cycles at ±0.80 strain amplitude (Figure 5.4). The austempered steel sample B15VA-2 reveals better fatigue life at all the strain amplitudes as depicted in Figure 5.4 and Table 5.1.

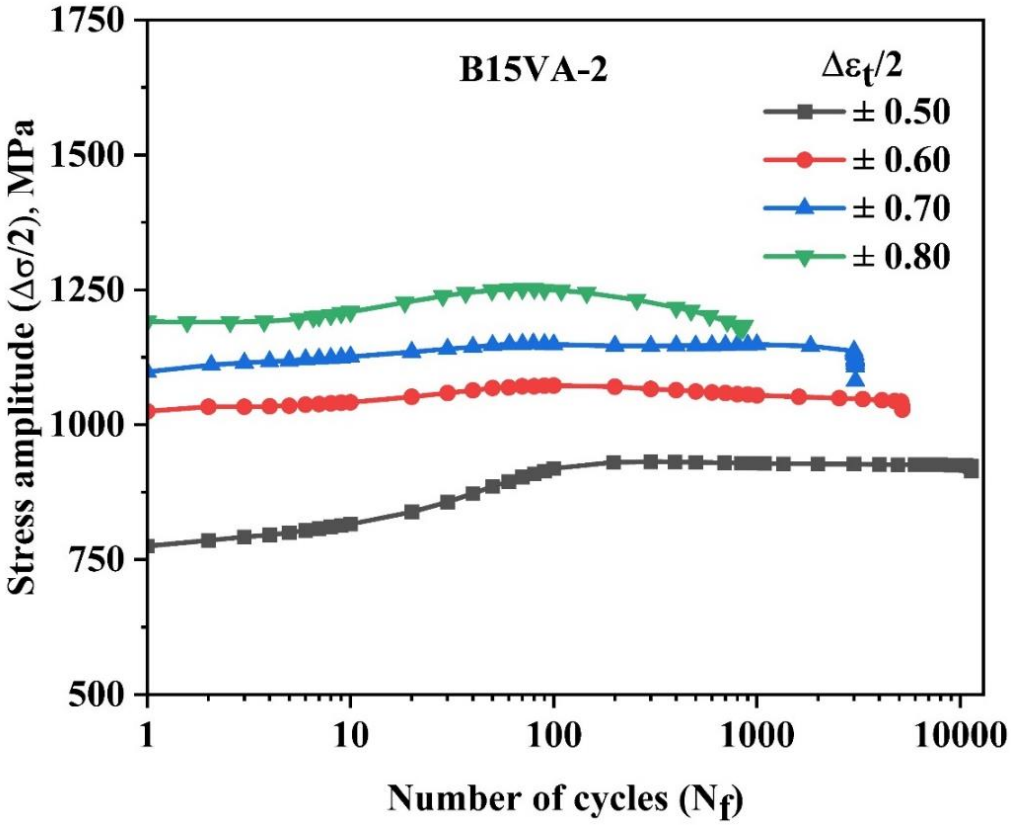

Figure 5.3 Cyclic stress response of austempered sample B15VA-2.

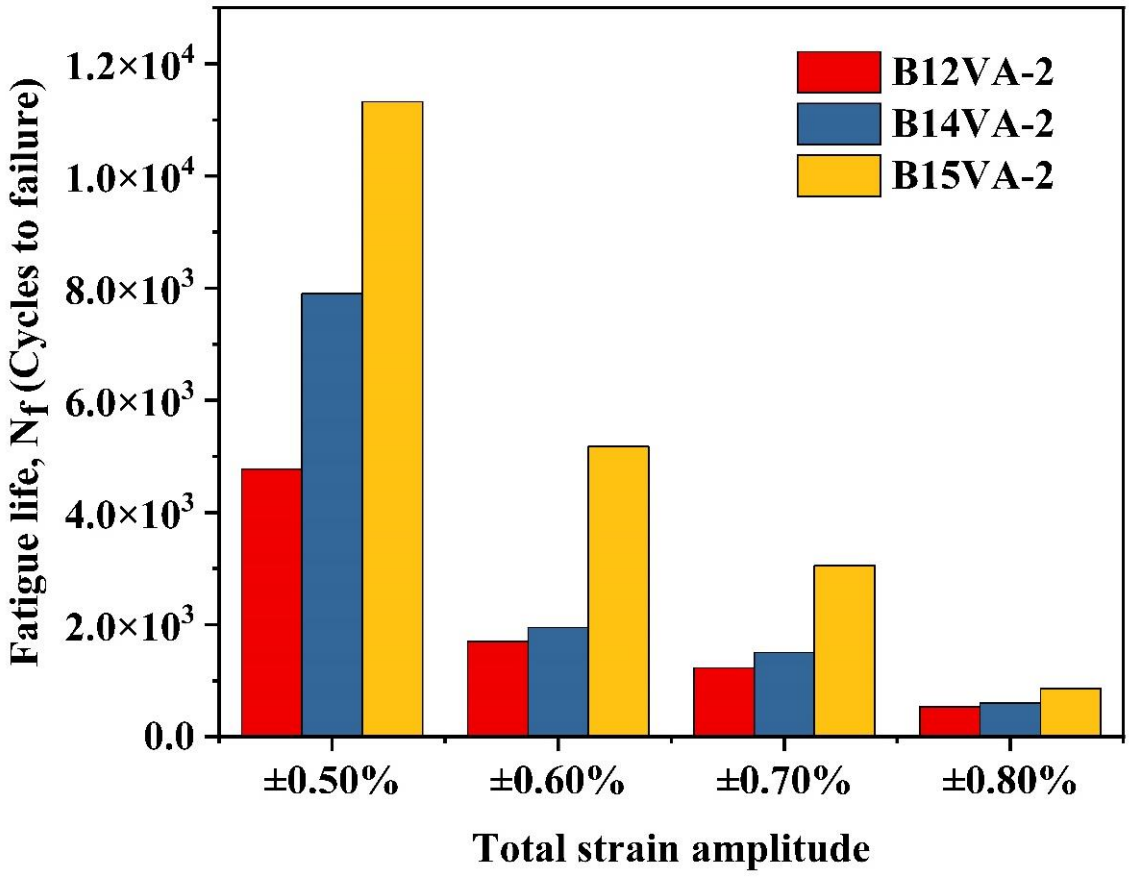

Figure 5.4 Fatigue life cycles for the austempered steel samples B12VA-2, B14VA-2 and B15VA-2 at different total strain amplitudes.

Table 5.1 Low cycle fatigue data of austempered samples B12VA-2, B14VA-2 and B15VA-2 at different total strain amplitudes.

Sr. No.	Total Strain Amplitude $\Delta\varepsilon_t/2 \times 10^{-2}$	Samples								
		B12VA-2			B14VA-2			B15VA-2		
		$\Delta\varepsilon_p/2 \times 10^{-2}$	$\Delta\varepsilon_e/2 \times 10^{-2}$	$2N_f$	$\Delta\varepsilon_p/2 \times 10^{-2}$	$\Delta\varepsilon_e/2 \times 10^{-2}$	$2N_f$	$\Delta\varepsilon_p/2 \times 10^{-2}$	$\Delta\varepsilon_e/2 \times 10^{-2}$	$2N_f$
1	±0.50	0.015	0.485	9554	0.035	0.465	15798	0.037	0.463	22644
2	±0.60	0.060	0.540	3398	0.075	0.525	3896	0.052	0.548	10354
3	±0.70	0.075	0.625	2456	0.148	0.552	3010	0.086	0.614	6102
4	±0.80	0.250	0.550	1078	0.135	0.665	1198	0.126	0.674	1728

The fatigue behaviour of the austempered steels B12VA-2, B14VA-2 and B15VA-2 is analyzed using the Coffin-Manson relationship, which relates the plastic strain amplitude ($\Delta\varepsilon_p/2$) to the number of reversals to failure (2Nf). The equation is given below [175]:

$$\frac{\Delta\varepsilon_p}{2} = \varepsilon'_f(2N_f)^c \qquad 5.1$$

Where, ε'_f is fatigue ductility coefficient and c fatigue ductility exponent. The Coffin-Manson (C-M) plots between log((Δεp/2) and log(2Nf) for the samples B12VA-2, B14VA-2 and B15VA-2 are depicted in Figure 5.5.

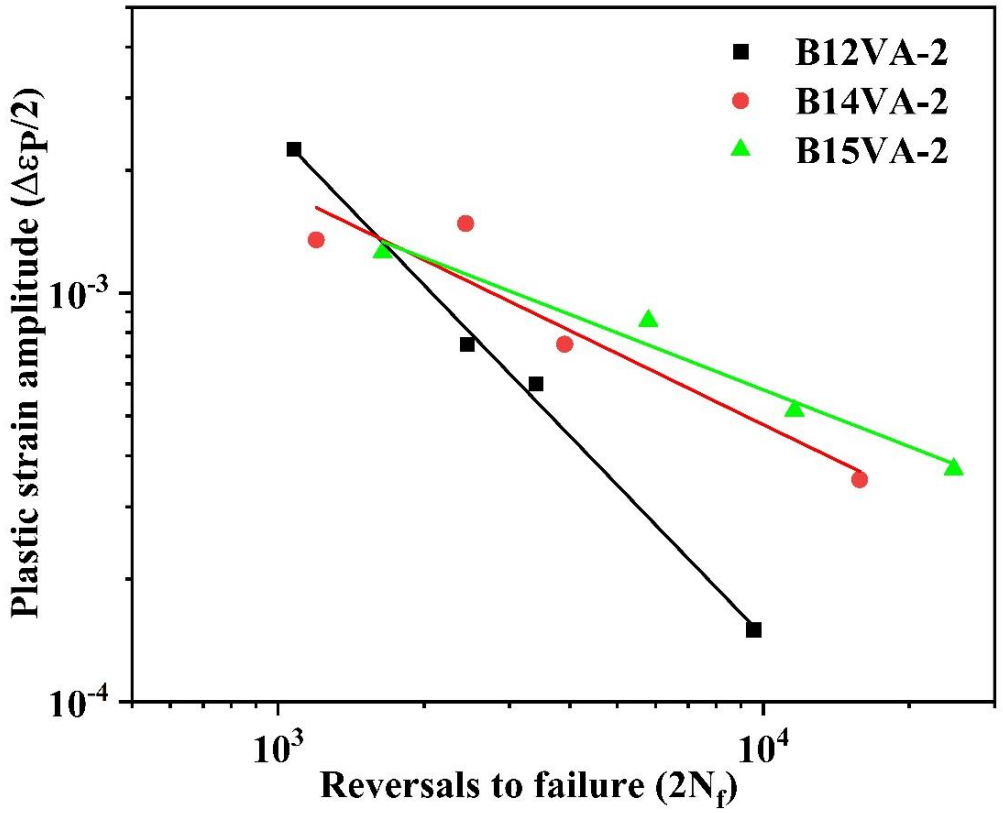

Figure 5.5 Coffin-Manson plots of the austempered samples B12VA-2, B14VA-2 and B15VA-2.

The low cycle fatigue parameters were determined by analyzing the Coffin-Manson plots depicted in Figure 5.5. Coffin-Manson plot for austempered sample B12VA-2, B14VA-2 and B15VA-2 were plotted for total strain amplitude of ±0.50, ±0.60, ±0.70 and ±0.80. The resulting values of these parameters are presented in Table 5.2. It was observed from Coffin-Manson plot that with decrease in magnitude of fatigue ductility exponent (c) (slope of Coffin-Manson plot), the fatigue life increases and the material B15VA-2 depict better fatigue life among the studied steels.

Table 5.2 Low cycle fatigue parameters calculated from Coffin-Manson plots of the austempered steels.

Samples	Fatigue ductility coefficient (ε'_f)	Fatigue ductility exponent (c)
B12VA-2	9.38	− 1.23
B14VA-2	0.45	− 0.76
B15VA-2	0.20	− 0.63

5.1.2 Fractography of the Fatigue Tested Sample

Fracture surfaces of the B12VA-2, B14VA-2, and B15VA-2 samples tested at different total strain amplitudes, from ±0.50% and ±0.80%, are shown in Figures 5.6 and 5.7, respectively. Figure 5.6a-c depicts the SEM SEIs of the fracture surface of B12VA-2, B14VA-2 and B15VA-2, respectively tested at ±0.50% strain amplitude. The crack initiation sites and crack propagation paths are marked with yellow dashed circles and yellow arrow, respectively. Crack initiation in all the studied samples was from the outer surface and single point crack initiation sites were observed. Figure 5.6d-f displays the magnified image of the selected area of the Figure 5.6a-c and reveals the presence of fine striations on the transgranular facets, which reveals the crack propagation of stage 2.

Figure 5.7a-c depict the SEIs of the fractured surface of the samples B12VA-2, B14VA-2 and B15VA-2 tested at ±0.80% strain amplitude. Similar type of fracture behaviour is observed at ±0.80 strain amplitude to that tested at ±0.50% strain amplitude but very limited striations were seen. Some of the secondary cracks were observed in all the samples tested at ±0.50% and ±0.80% strain amplitudes. The rate of crack propagation was higher for ±0.80% strain amplitude than that of ±0.50%.

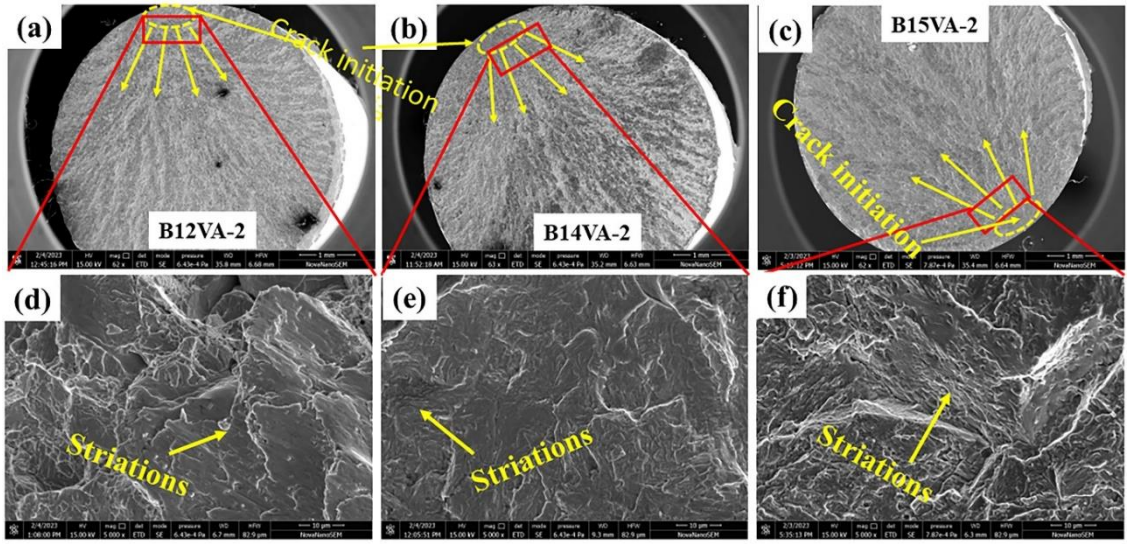

Figure 5.6 SEM fractographs showing the fracture surface tested at strain amplitude of ±0.50% (a) B12VA-2, (b) B14VA-2 and (c) B15VA-2. (d), (e) and (f) reveals the magnified images of red color rectangle of (a), (b) and (c), respectively.

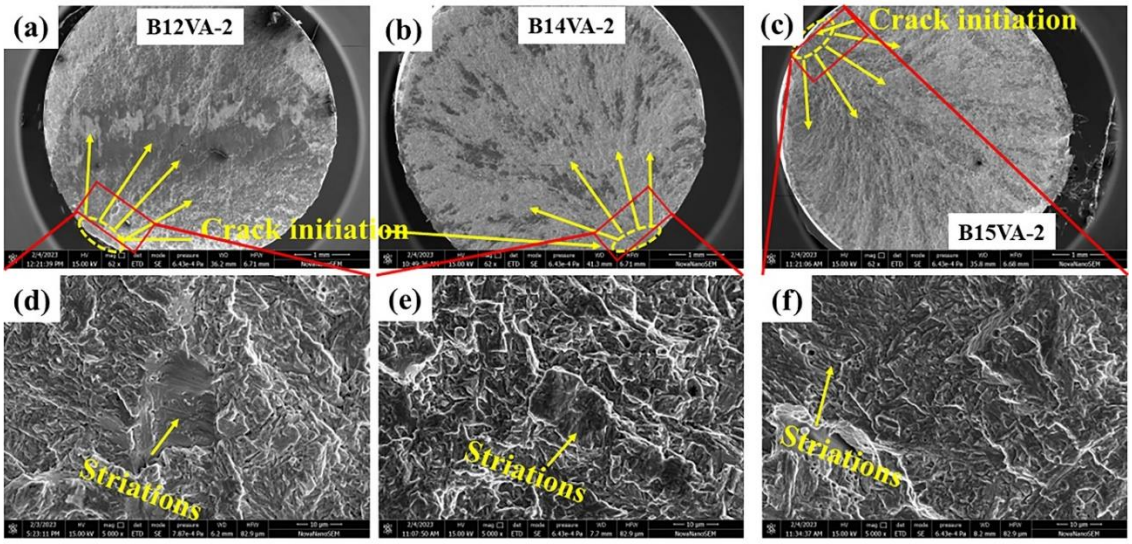

Figure 5.7 SEM fractographs showing the fracture surface tested at strain amplitude of ±0.80% (a) B12VA-2, (b) B14VA-2 and (c) B15VA-2. (d), (e) and (f) reveals the magnified images of red color rectangle of (a), (b) and (c), respectively.

The X-ray diffraction studies of the fatigue samples tested at ±0.50% strain amplitude of the austempered steels B12VA-2, B14VA-2 and B15VA-2 are depicted in Figure 5.8. X-ray diffraction pattern of B12VA-2 sample reveals the presence of new phase α′ martensite along with retained austenite and bainite. If compared this X-ray diffraction pattern with that of the austempered B12VA-2 (discussed in Chapter 3), there is marginal reduction in the peak intensity of the retained austenite, due to formation of new phase (strained-induced martensite) during cyclic loading. Similar type of pattern is observed for fatigue fractured B14VA-2 and B15VA-2 samples. The formation of strain-induced martensite during cyclic loading contributed to the cyclic hardening behaviour.

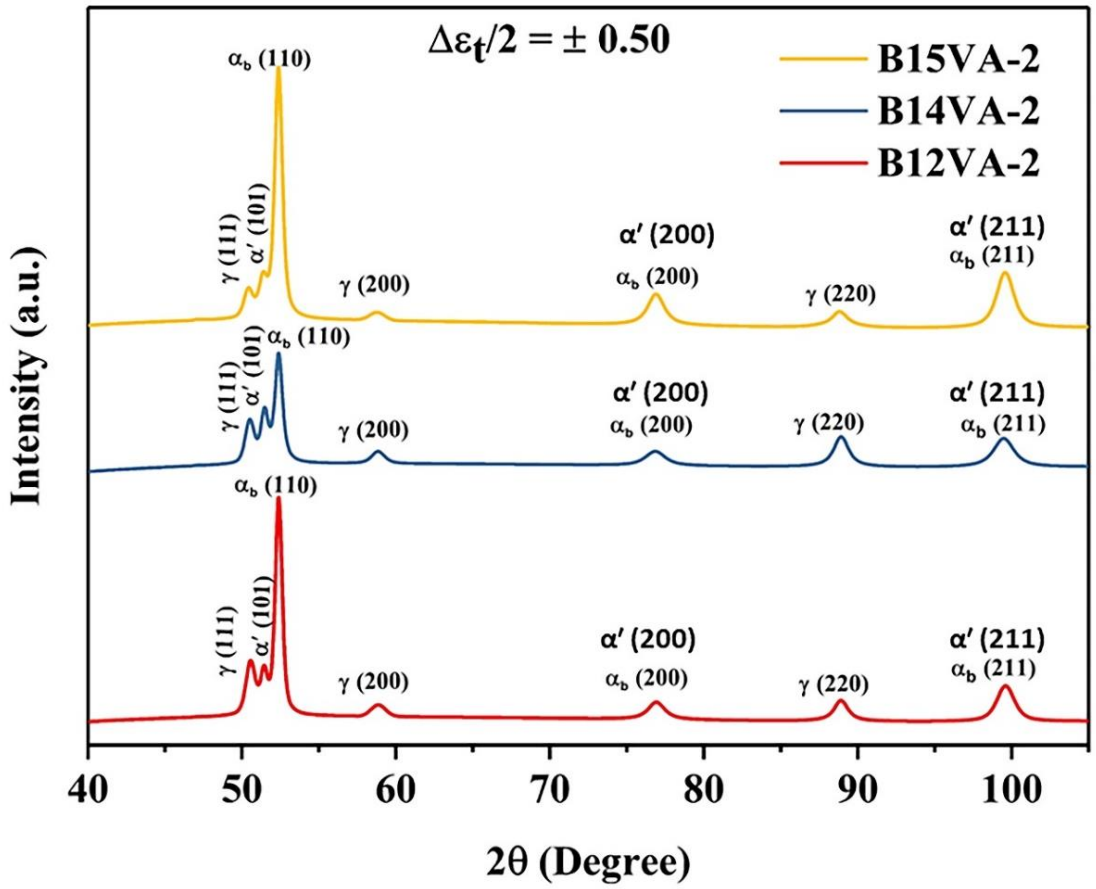

Figure 5.8 X-ray diffraction studies of fatigue tested samples.

5.2 CHARPY IMPACT BEHAVIOUR

The impact energy of the Charpy impact austempered samples tested at -40°C, 0°C and room temperature (RT) are depicted in Figure 5.9 and Table 5.4. The impact energy of sample B12VA-1 at RT, 0°C and -40°C are 12.1±0.1 J/cm^2, 7.7±0.1 J/cm^2 and 4.1±0.1 J/cm^2, respectively. Sample B12VA-2 depicts the impact energy of 10.5±0.1 J/cm^2, 6.5±0.2 J/cm^2 and 4.5±0.1 J/cm^2 at RT, 0°C and -40°C, respectively. Material B14VA-1 shows the impact energy of 11.2±0.2 J/cm^2, 9.6±0.1 J/cm^2 and 7.5±0.1 J/cm^2 tested at RT, 0°C and -40°C, respectively. The impact energy of B14VA-2, tested at RT, 0°C and -40°C are 14.9±0.2 J/cm^2, 9.8±0.1 J/cm^2, and 7.0±0.2 J/cm^2, respectively. The impact energy of B14VA-2 at RT is significantly higher than that of B14VA-1.

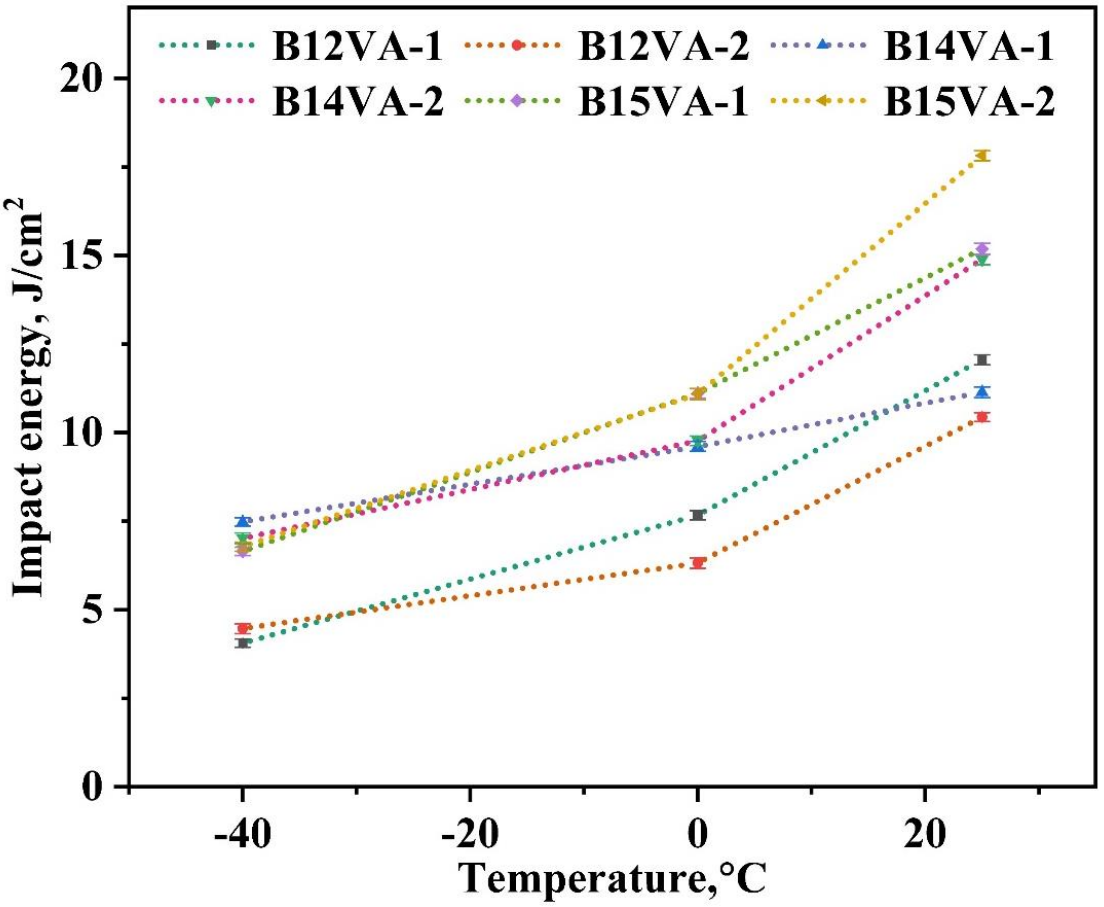

Figure 5.9 Variation of Charpy impact energy of austempered steels B12VA-1, B12VA-2, B14VA-1, B14VA-2, B15VA-1 and B15VA-2 with temperature.

The Charpy impact energy of the sample B15VA-1 tested at RT, 0°C and -40°C are 15.2±0.2 J/cm^2, 11.1±0.1 J/cm^2, and 6.7±0.1 J/cm^2, respectively. With increasing austempering time the impact energy of B15VA-2 sample at RT increases and the impact energy at RT, 0°C and -40°C are 17.8±0.1 J/cm^2, 11.1±0.2 J/cm^2, and 6.8±0.1 J/cm^2, respectively. There is no significant change in the Charpy impact energy with the austempering time at sub-zero temperatures of 0°C and -40°C (Table 5.4).

Table 5.3 Charpy impact energy of the austempered steels.

Samples	Impact energy (J/cm^2)		
	-40°C	0°C	RT
B12VA-1	4.1±0.1	7.7±0.1	12.1±0.1
B12VA-2	4.5±0.1	6.5±0.2	10.5±0.1
B14VA-1	7.5±0.1	9.6±0.1	11.2±0.2
B14VA-2	7.0±0.2	9.8±0.1	14.9±0.2
B15VA-1	6.7±0.1	11.1±0.1	15.2±0.2
B15VA-2	6.8±0.1	11.1±0.2	17.8±0.1

5.2.1 Fractography of the Charpy Impact Tested Sample

SEM secondary electron images of central region of the Charpy impact fracture surface of the austempered samples were shown in the Figure 5.10 and Figure 5.11. Figure 5.10a-f depicts the SEIs of the room temperature impact tested samples B12VA-1, B12VA-2, B14VA-1, B14VA-2, B15VA-1 and B15VA-2, respectively. Fracture surface of B12VA-1 reveals the colonies of cleavage fracture facets separated by heavy ridges which is a typical characteristic of quasi-cleavage fracture. Some of the secondary cracks were observed on the surface. Similar type of fracture surface was observed for B12VA-2, B14VA-1 and B14VA-2. Sample B15VA-1 depicts very fine size micro-dimples along with cleavage facets surrounded by heavy ridges and the sample B15VA-2 shows similar fracture surface to B12VA-1 but very limited fine sized micro-dimples.

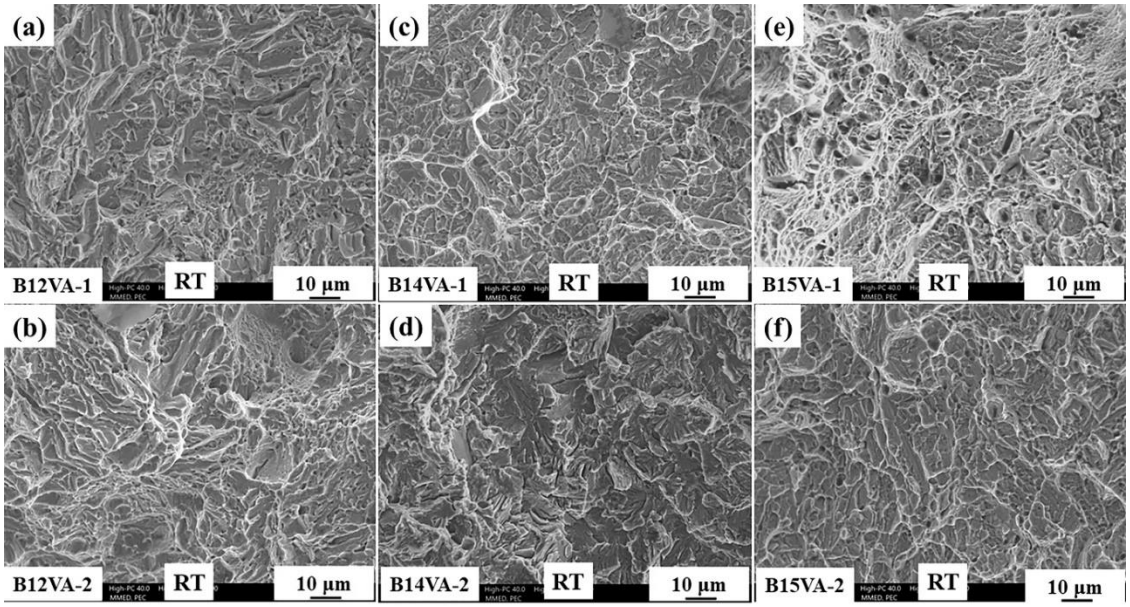

Figure 5.10 Fractographs of the Charpy impact tested austempered steels at room temperature: (a) B12VA-1, (b) B12VA-2, (c) B14VA-1, (d) B14VA-2, € B15VA-1 and (f) B15VA-2.

Figure 5.11a-f displays the fracture surface of -40°C Charpy impact tested samples of B12VA-1, B12VA-2, B14VA-1, B14VA-2, B15VA-1 and B15VA-2, respectively. It resembles similar fracture behaviour to that of room temperature tested samples but the large number of secondary cracks were observed in B12VA-1, B12VA-2, B14VA-1 and B14VA-2 but the micro-sized dimples were not seen in B15VA-1 and B15VA-2 samples. Increased fraction of cleavage facets and ridges to that of RT tested samples were seen. This kind of brittle fracture characteristic is directly related to poor toughness for Charpy impact.

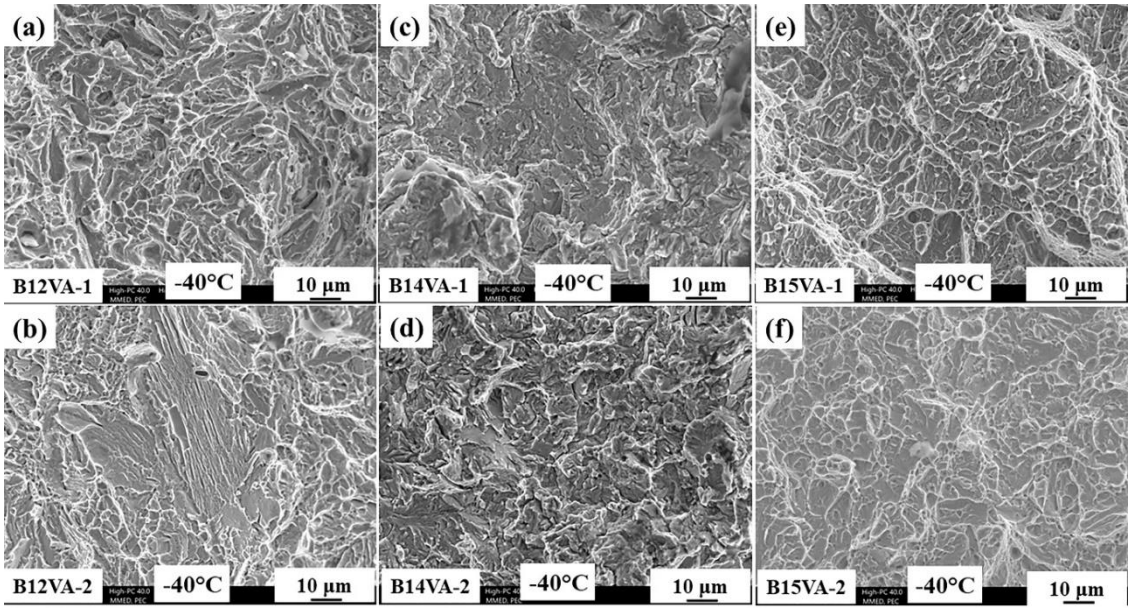

Figure 5.11 Fractographs of the Charpy impact tested austempered steels at -40°C: (a) B12VA-1, (b) B12VA-2, (c) B14VA-1, (d) B14VA-2, (e) B15VA-1 and (f) B15VA-2.

5.2.2 X-ray Diffraction Studies of Charpy Impact Tested Samples

XRD measurements were conducted to investigate any potential microstructural changes resulting from the Charpy impact test. Figure 5.12a-f depicts the X-ray diffraction patterns of the Charpy impact tested samples B12VA-1, B12VA-2, B14VA-1, B14VA-2, B15VA-1 and B15VA-2. X-ray diffraction pattern displays the presence of new phase peak of body centered tetragonal (BCT) martensite (α′ martensite) along with retained austenite and bainite. During impact loading majority of blocky retained austenite transformed to strained-induced martensite, which led to a brittle fracture. XRD pattern of Charpy impact fractured samples are compared with that of austempered samples (Chapter 3), and the peak intensity of retained austenite reduced significantly in all the samples.

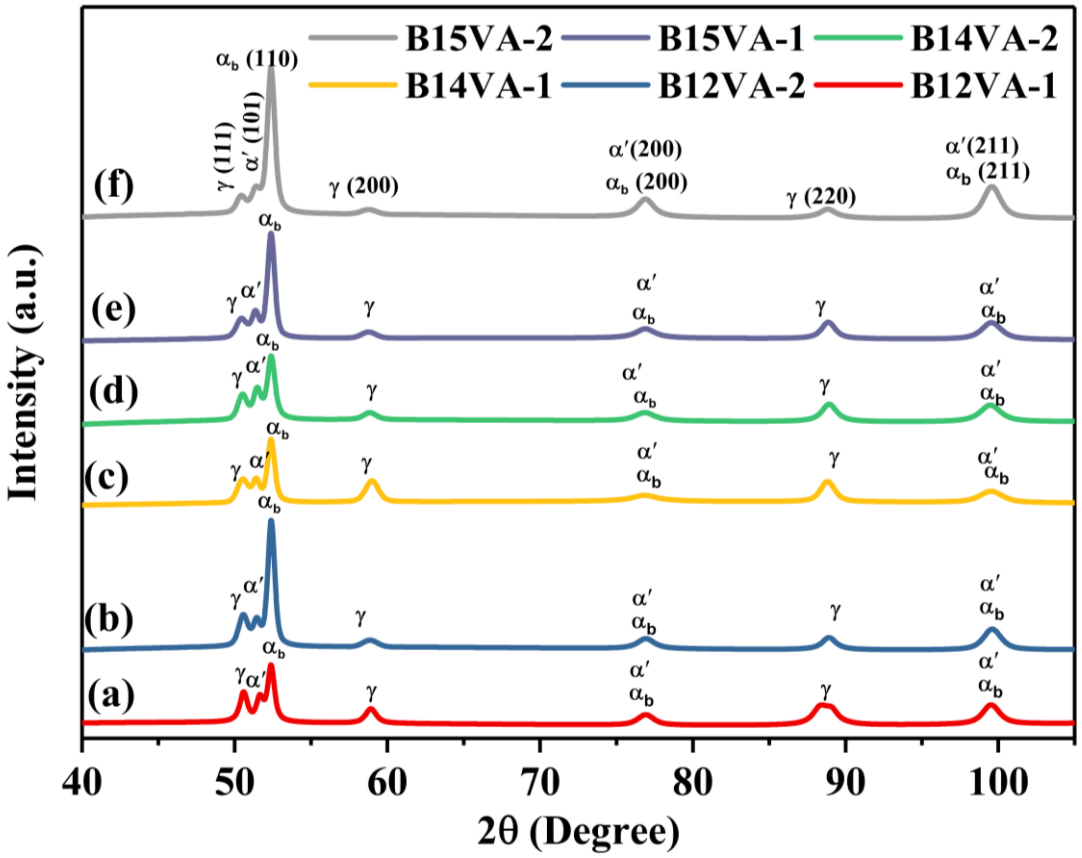

Figure 5.12 X-ray diffraction pattern of the Charpy impact tested austempered samples: (a) B12VA-2, (b) B12VA-2, (c) B14VA-2, (d) B14VA-2, (e) B15VA-1 and (f) B15VA-2.

5.3 DISCUSSION

5.3.1 Low Cycle Fatigue Behaviour

The samples of B12VA-2, B14VA-2 and B15VA-2 were austempered at 250°C temperature for 96 h, 48 h and 50 h, respectively to get ~35% retained austenite and ~65% nanostructured bainite. Retained austenite is of two forms, filmy and blocky, in all the materials (as discussed in chapter 3). The size and distribution of filmy and blocky austenite are quite different in the austempered samples. Also, the thickness of nanostructured bainite plate varied for the samples B12VA-2, B14VA-2 and B15VA-2 (discussed in chapter 3). The size and distribution of filmy retained austenite, blocky retained austenite and nanostructured bainite led to varying mechanical properties such

as hardness, tensile properties (discussed in chapter 4), fatigue behaviour and impact behaviours.

The cyclic stress response of austempered samples of B12VA-2, B14VA-2, and B15VA-2 displays distinct behaviour, characterized by cyclic hardening and softening phenomena at both low and high strain amplitudes. At low strain amplitudes, the samples initially undergo cyclic hardening, followed by cyclic saturation and eventual softening. This behaviour may be attributed to several factors, such as the transformation of retained austenite to martensite, as well as dislocation tangling and/or dislocation multiplications. The presence of strain-induced martensite within the microstructure contributes to the observed cyclic hardening effects. On the other hand, at high strain amplitudes, the samples exhibit early cyclic hardening followed by cyclic softening, leading to failure. This behaviour is likely caused by dislocation rearrangements and annihilations [70]. Overall, the cyclic stress response is influenced by the interplay of various mechanisms, including phase transformations, dislocation dynamics, and the presence of strain-induced martensite.

The transformation of retained austenite to martensite in the austempered samples, as indicated by Figure 5.8, exhibits variation based on the chemical stability of the materials at different strain amplitudes. This observation aligns with findings reported in the literature [67]. It suggests that the strain-induced transformation of austenite to martensite plays a significant role in the initial cyclic hardening behaviour observed in the samples. Additionally, the tangling of dislocations, which restricts the mobility of pre-existing mobile dislocations within the original microstructure, is another factor contributing to cyclic hardening. The combined effects of strain-induced austenite-to-

martensite transformation and dislocation tangling contribute to the overall cyclic hardening response observed in the austempered samples.

At various plastic strain amplitudes, the B15VA-2 sample exhibits an obvious longer fatigue lifetime than the B12VA-2 and B14VA-2 samples. It is noted that the B15VA-2 sample has smaller size and uniform distribution of blocky austenite than that of B12VA-2 and B14VA-2 samples. Meanwhile, the sample of B15VA-2 having higher hardness and tensile strength than that of B12VA-2 and B14VA-2, led to better fatigue life due to the formation of more strain-induced martensite in B15VA-2 than B12VA-2 and B14VA-2 samples.

In this investigation, it was observed that at low total strain amplitudes, the fatigue lifetime of steels B15VA-2 (0.98% C), B14VA-2 (1.02% C), and B12VA-2 (1.18% C) decreased as the initial carbon percentage in the steels increased. Notably, the fatigue lifetime of the B15VA-2 sample was higher than that of the B14VA-2 and B12VA-2 samples. However, at high total strain amplitudes, the three samples exhibited minimal variation in fatigue lifetime or even demonstrated a contrary trend to what observed at low strain amplitudes. The following analysis aims to systematically examine and discuss the specific reasons behind these observations. The total fatigue lifetime is well known to consist of two key components: crack initiation and propagation lifetimes. At low total strain amplitudes, the accumulated plastic strain remains relatively small due to the smaller plastic strain induced during each cycle. Elastic strain dominates the total strain in such circumstances. As a result, the crack initiation lifetime primarily determines the overall fatigue lifetime. During the fatigue cycling process, the retained austenite undergoes a transformation into martensite, particularly within the blocky retained

austenite regions. In a material with multiple phases like this, the presence of incoherent interfaces between the phases can facilitate fatigue cracking at these interfaces. Conversely, continuous cycling leads to the formation of brittle martensite grains, which are characterized by their hardness and brittleness. These grains must then withstand the plastic deformation of the untransformed ductile retained austenite. Consequently, this results in inhomogeneous deformation between the two phases [176-180]. Consequently, the localized inhomogeneous deformation can create stress and strain concentrations within the blocky austenite or at the interface of the martensite and austenite. These areas are more prone to the initiation of micro-voids and cracks, thereby shortening the crack initiation lifetime. The findings of the investigation indicate that at low strain amplitudes, the fatigue lifetime is predominantly influenced by crack initiation. The presence of incoherent interfaces and the inhomogeneous deformation between the martensite and retained austenite phases contribute to the initiation of micro-voids and cracks, leading to a decrease in the crack initiation lifetime. These factors explain the observed reduction in fatigue lifetime with an increase in the initial carbon percentage in the examined steels.

The presence of larger blocky austenite in the B12VA-2 and B14VA-2 samples, compared to the B15VA-2 sample, results in a faster transformation of blocky retained austenite into martensite. This accelerated transformation process leads to the formation of a higher number of micro-voids/cracks, primarily concentrated in the blocky austenite region. Consequently, the B12VA-2 and B14VA-2 samples are expected to exhibit a shortened total fatigue lifetime at low total strain amplitudes compared to the B15VA-2 sample. As the total strain amplitude increases, the accumulated plastic deformation progressively rises, further accelerating crack initiation and reducing the proportion of

initiation lifetime in the overall fatigue life. At high strain amplitudes, the dominant factor determining fatigue lifetime shifts to crack propagation lifetime. Previous studies indicate that the newly formed martensite, resulting from the transformation, acts as a fast propagation path for fatigue cracks due to its brittle characteristics [181-183]. Additionally, the martensite transformation from retained austenite predominantly occurs in regions of severe plastic deformation around the crack tip, caused by higher stress concentration during crack propagation [184,185]. This process triggers the Transformation-Induced Plasticity (TRIP) effect, which absorbs significant amounts of plastic deformation energy, leading to stress relaxation at the crack tip and delaying crack propagation. Furthermore, when the fatigue crack intersects bainitic ferrite regions, it consumes substantial plastic deformation energy through the severe twisting or fracturing of ductile film-like retained austenite and bainite laths.

5.3.2 Charpy Impact Toughness

The observed fracture surfaces exhibit colonies of cleavage fracture facets that are separated by prominent ridges, which is a distinctive characteristic of quasi-cleavage. This observation aligns with the findings of previous studies [51, 72, 186]. It has been observed that nanostructured bainitic steels exhibit transformation-induced plasticity (TRIP) in tensile tests, where retained austenite undergoes martensite transformation during plastic deformation [60, 187]. However, in the current study, strain-induced martensite was also observed on the fracture surface of Charpy impact samples, but it did not result in the TRIP effect. Several factors may be connected to this corresponding fracture mechanism and the decrease in impact toughness. Unlike the tensile samples, it is challenging to define a percolation threshold for fracture in the Charpy samples, where the remaining austenite becomes geometrically isolated, leading to fracture. This

discrepancy can be attributed to the significantly faster deformation rate and more localized strain experienced during Charpy impact loading, with a typical strain rate of 10^2 s^{-1}, compared to the range of 10^{-2}–10^{-4} s^{-1} used in tensile tests. It is important to note that during Charpy impact loading, the formation of brittle martensite occurs directly in front of the crack tip. The crack mainly follows interlath paths, initially propagating through ductile austenite, which is expected to absorb impact energy through plastic deformation. However, this viewpoint contradicts the exceptionally low impact toughness observed in the present Charpy impact results. To explain the crack propagation process during Charpy impact loading, the following depiction appears appropriate:

As the crack propagates, there is a significant strain concentration in the localized area ahead of the advancing crack tip. Simultaneously, the retained austenite undergoes a transformation into strained-induced martensite. Consequently, only brittle phases are present in the vicinity of the crack tip, allowing for unhindered crack propagation. The successive martensitic transformation significantly accelerates the progression of brittle fracture, resulting in extremely low impact toughness of the material. Nanostructured bainitic ferrite is known to have a supersaturated carbon content (~0.2 wt.%) [172, 188-195] and high dislocation densities [196], making it highly unlikely for significant deformation via dislocation glide to occur during Charpy impact loading.

Within this strained zone, there is no presence of a soft phase, and plastic deformation cannot occur. Consequently, the advancing crack tip cannot be blunted, impeding crack propagation. As the crack continues to propagate, strain-induced martensitic transformation persists ahead of the crack tip, eventually leading to brittle

fracture through cleavage. Twinned martensite, compared to bainitic ferrite, is more susceptible to crack propagation, which explains the prevalence of interlath cracks. Thus, the inherent low impact energy of nanostructured bainite becomes an unavoidable disadvantage

5.4 CONCLUSIONS

1. Fatigue life decreases with increasing strain amplitude. B15VA-2 steel revealed best fatigue life (11322 cycles) amongst the studied steel and cyclic hardening was observed at all the strain amplitudes for all the steels.
2. XRD studies of fatigue tested samples revealed the formation of new phase, martensite. During cyclic loading, blocky retained austenite which is chemically stable but mechanically unstable, is transformed to martensite and contributed to cyclic hardening.
3. The crack initiation takes place at the surface in all the fatigue tested samples. The fracture surface reveals striations, which are very fine and are visible on transgranular facets.
4. B15VA-1 and B15VA-2 samples reveal better Charpy impact energy of 15-18 J/cm^2. Charpy impact samples reveal typical quasicleavage fractographs, indicating a specific pattern of fracture morphology. The crack propagation predominantly occurred through interlath cracking, suggesting a specific mechanism of crack growth within the material.